ACCSCIENCE PUBLISHING

International Journal of Bioprinting

RESEARCH ARTICLE

Optimal structural characteristics of bone tissue engineering scaffolds from bionics and PSO-BP-NSGA III integrated algorithm

Yuxi Liu[1,2†*], Aihua Li[3†], Hong Sun[1], Shuge Li[1], and Song Chen[4]

[1] School of Smart Health, Chongqing Polytechnic University of Electronic Technology, Chongqing, China

[2] College of Mechanical and Vehicle Engineering, Chongqing University, Chongqing, China

[3] Department of Gastroenterology, Chongqing University Cancer Hospital, School of Medicine, Chongqing University, Chongqing 400030, China

[4] College of Mechanical Engineering, Chongqing University of Technology, Chongqing, China

Abstract

The repair of large segmental bone defects has always been a significant challenge in clinical practice, with stress shielding being one of the key issues. Here, tree-like fractal biomimetic scaffolds were created based on the morphological similarity between natural trees and bone trabeculae. To optimize the balance between high yield strength and low elastic modulus of the scaffold, an integrated particle swarm optimization-backpropagation-non-dominated sorting genetic algorithm III (PSO-BP-NSGA III) was employed. The scaffolds were fabricated using selective laser melting three-dimensional printing with Ti6Al4V, and their mechanical performance was experimentally evaluated and compared with the algorithm's predictions. The tree-like fractal scaffold exhibited a radial gradient in porosity, similar to that of natural bone. The second-order fractal scaffold achieved an effective synergy between yield strength and Young's modulus, demonstrating high yield strength and low Young's modulus. Additionally, it showed a favorable fluid flow gradient and permeability, with a comprehensive permeability of 3.13×10^{-8} m^2. The relative errors between the test and predicted values of yield strength and Young's modulus were 0.83% and 7.93% respectively, indicating that the PSO-BP-NSGA III integrated algorithm has good predictive ability. These findings establish a validated bionic design framework that integrates advanced optimization algorithms to guide the development of bone tissue engineering scaffolds.

***Keywords*:** Integrated algorithm; Multi-objective optimization; Stress shielding; Tree-like fractal scaffold; Young's modulus

†These authors contributed equally to this work.

***Corresponding author:**
Yuxi Liu (liuyuxi@cqcet.edu.cn)

Citation: Liu Y, Li A, Sun H, Li S, Chen S. Optimal structural characteristics of bone tissue engineering scaffolds from bionics and PSO-BP-NSGA III integrated algorithm. *Int J Bioprint*. 2025;11(6):451-471. doi: 10.36922/IJB025380381

Received: September 15, 2025
Revised: October 19, 2025
Accepted: October 25, 2025
Published Online: October 27, 2025

1. Introduction

Large segmental bone defects have long been a significant challenge in clinical practice,[1] often leading to complications such as nonunion and implant failure.[2] Stress shielding is one of the primary reasons for the failure of bone implants, usually due to the implant's stiffness exceeding that of the adjacent bone, leading to bone resorption around the

prosthesis.[3,4] According to clinical research, more than 15% of patients require revision surgery after total hip replacement, of which approximately 33% are directly related to implant loosening caused by stress shielding.[5] To address this challenge, there is an urgent need to conduct in-depth research on the balance between the structure, function, and mechanical properties of bone implants.

In recent years, as the core carrier of bone tissue engineering, the design and optimization of porous bone scaffolds have mainly focused on mechanical properties, biological activity, and manufacturing accuracy.[6] In terms of biomimetic structural innovation, the three-period minimal surface (TPMS) has emerged as a research hotspot due to its continuous curvature, high specific surface area, and bone trabecular-like characteristics.[7,8] For example, the I-WP type TPMS scaffold can achieve a gradient distribution of porosity ranging from 68.01% to 96.48%.[9] The Voronoi structure scaffold has a wall shear stress ratio of 34.68%, which is closer to the fluid environment of natural bone trabeculae.[10] The application of multi-objective optimization algorithms has promoted the precise regulation of scaffold performance.[11,12] The application of machine learning (ML) and genetic algorithms can effectively improve the reverse design accuracy of porous scaffolds.[13] In addition, the innovative application of ML and optimization algorithms in bone tissue helps to enhance the osteoinductive capacity of scaffolds,[14] optimize the mechanobiological properties of scaffolds,[15] and achieve a leap from limited results to infinite theoretical results.[16] The breakthrough of additive manufacturing (AM) technology has provided the possibility for the realization of complex structures.[17] New-type scaffolds based on AM can meet the mechanical requirements of cancellous bone,[18] enhance compressive strength[19] and biomineralization ability,[20] and guide the transformation of the immune microenvironment toward promoting bone regeneration.[21] Furthermore, the radial gradient porosity prepared via three-dimensional (3D) printing closely resembles the hierarchical structure of human bones.[22]

The material and mechanical properties of porous scaffolds are key factors that determine their clinical effectiveness and directly affect stability and regeneration efficiency.[23] With the popularization of 3D printing technology and breakthroughs in materials science, the mechanical design of porous scaffolds has evolved from a single "modulus matching" to "structure–function collaborative optimization."[24] TPMS magnesium alloy scaffolds help to enhance early cell adhesion and proliferation capabilities,[25] and the Si–OH groups in Ti_3SiC_2 ceramic scaffolds are beneficial for promoting the mineralization rate of apatite.[26] The structural optimization of bone scaffolds can effectively reduce the risk of stress shielding and improve the permeability of the scaffold,[27] and the porosity and specific surface area of the scaffold directly affect the ability of bone regeneration.[28] The strut-type bionic scaffold with a negative Poisson's ratio is also an effective means of reducing the stress-shielding effect of implants.[29] Permeability refers to the ability of fluid to transmit within porous media, which is a core performance index of bone scaffolds. It directly affects nutrient diffusion and vascular network formation, thereby determining the efficiency of bone regeneration.[30] There is an inherent contradiction between the high permeability and mechanical strength of porous scaffolds: increasing porosity enhances permeability but reduces scaffold strength.[31] Therefore, while improving the permeability of the scaffold, its mechanical strength must also be taken into account. In existing studies, the primary methods to enhance permeability include the optimal design of porous scaffold structures[32–34] and the development of novel porous materials.[35]

Reducing the stiffness of porous bone implants while maintaining sufficient strength to withstand loads during daily activities is a key challenge in their design. Currently, research on bone implants mainly attempts to reduce stress shielding through methods such as pore optimization,[8,18] material development,[25,26] and structural bionics,[13,27] but the effects are limited. Moreover, research on the synergy between the structure, function, and mechanical properties of porous scaffolds is severely insufficient. Based on this, this study aims to reduce stress shielding in porous scaffolds and achieve a balance between their structure, modulus, and strength. A combined approach of computer-integrated algorithms, mechanical experiments, finite element (FE) calculations, and computational fluid dynamics (CFD) simulation calculations was adopted to perform multi-objective optimization on the structural parameters of tree-like fractal scaffolds. Firstly, based on the morphological similarity between natural trees and bone trabeculae, biomimetic design of tree-like fractal scaffolds and theoretical analysis were completed. Secondly, through 3D printing preparation, mechanical testing, FE analysis, and CFD permeability simulation, a fractal structure model with excellent mechanical properties and permeability was determined, and the feasibility and accuracy of the FE calculation were verified. Then, through orthogonal design and FE calculation, a dataset for multi-objective optimization calculation was obtained. The integrated particle swarm optimization-backpropagation-non-dominated sorting genetic algorithm III (PSO-BP-NSGA III) algorithm was used to complete the multi-objective optimization of the tree-like fractal scaffold, and the Pareto optimal solution set was obtained. Finally,

the scaffold structure parameters corresponding to the optimal solution were selected, and the porous scaffold was prepared and mechanically tested. The feasibility and correlation of the multi-objective optimization algorithm were verified by comparing the obtained results. This research provides theoretical and practical guidance for the structure design optimization and stress shielding reduction of novel porous bone scaffolds.

2. Materials and methods

The study's workflow is illustrated in Figure 1.

2.1. Design and analysis of the tree-like fractal scaffold

In response to the personalized needs of porous bone scaffolds for the repair of large segmental bone defects in clinical practice, this study focuses on the structural design and characteristic optimization of tree-like fractal biomimetic bone scaffolds. The goal is for their structure and performance to be optimized to closely resemble those of natural bone, while minimizing stress shielding. A systematic study was conducted on the synergistic effects among their structure, function, and mechanical properties.

The schematic diagram of the design process for the bionic scaffold with a radial gradient tree-like fractal structure is shown in Figure 2. The human bone has a radially gradient porous structure (Figure 2A).[36] The inner part is cancellous bone with high porosity (50–90%) to reduce weight and facilitate nutrient transport, while the outer part is cortical bone with low porosity, which can bear loads.[37] Based on the similarity between the branching structure of natural trees and the morphology of bone trabeculae,[38] four different tree-like fractal curves were designed, respectively, as shown in Figure 2B. By enabling tree-like fractal structures to grow radially and to array circumferentially, a porous structure with radial porosity gradients was designed (Figure 2C). Clinically, according to the specific bone defect site of the patient and the corresponding porosity distribution, a unique porous scaffold can be designed by optimizing the fractal curves. Firstly, according to the size of the bone defect site, the outer diameter D, inner diameter d, and height H of the implant (Figure 2D) were determined. Secondly, based on the radial distribution of porosity at the site of the bone defect, fractal curves were designed and fractal parameters were determined to complete the structural design of a concentric ring-shaped bone matrix (Figure 2E) and a radial tree-like trabecular network (Figure 2F). Then, the bone matrix and trabecular layers were alternately stacked along the axial direction to form a porous scaffold (Figure 2G). The axial structure of the second-order fractal biomimetic bone scaffold is shown in Figure 2H. Finally, a crisscross structure was used to connect and fix the bone matrix and trabecular layers (Figure 2I). To calculate the radial distribution of porosity of the scaffolds, the biomimetic scaffold was divided into regions a, b, c, d,

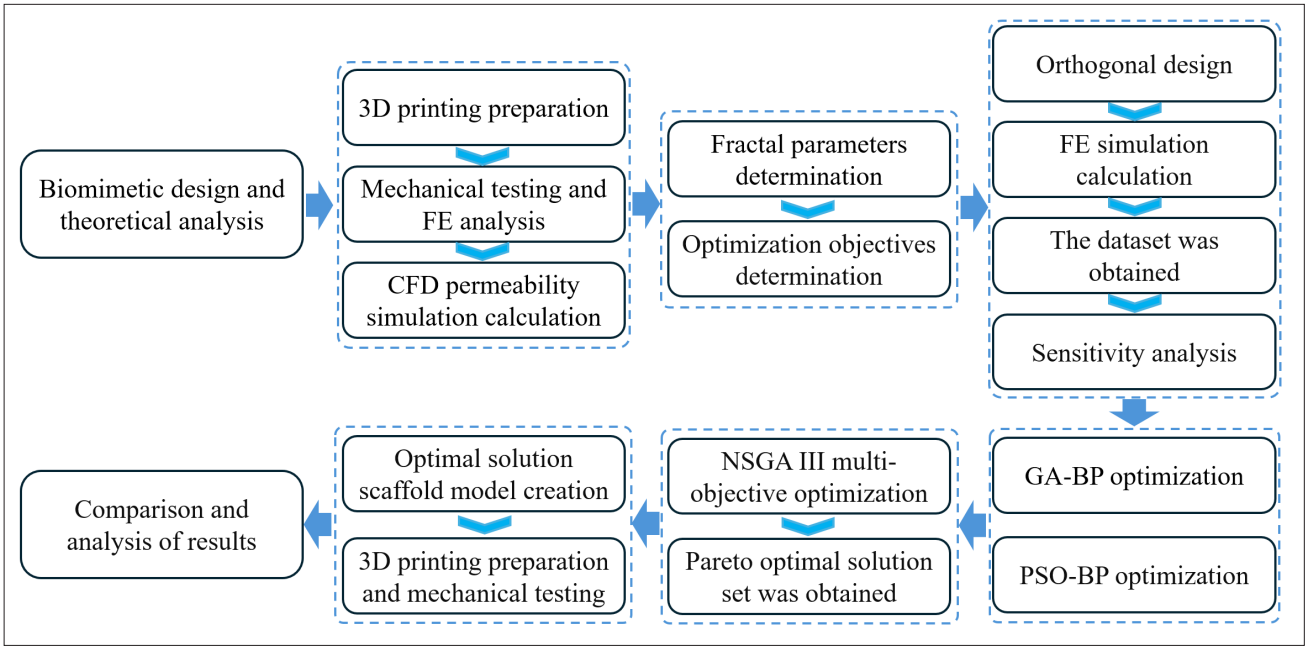

Figure 1. Workflow diagram. Abbreviations: 3D, three-dimensional; BP, backpropagation; CFD, computed fluid dynamics; FE, finite element; GA, genetic algorithm; NS, non-dominated sorting; PSO, particle swarm optimization.

and e along the radial direction with the centers of adjacent concentric rings as boundaries (Figure 2J).

The fractal parameters directly determine the pore size and the distribution of porosity in the tree-like fractal scaffold. The theoretical porosity calculation for the tree-like fractal scaffold was established in this study. The length ratio γ and diameter ratio μ of the j-th and (j-1)-th order trabeculae were calculated using **Equation (1)**:

$$\gamma = \frac{l_j}{l_{j-1}}, \mu = \frac{d_j}{d_{j-1}}, j = 1,2,3,\cdots,n \quad (1)$$

where N is the order of the tree-like fractal bone trabeculae; l_j and l_{j-1} are the lengths of the j-th and (j-1)-th order bone trabeculae, and d_j and d_{j-1} are their corresponding diameters.

The volume V_m of concentric ring bone matrix was calculated using **Equation (2)**:

$$V_m = \sum_{i=1}^{N} V_{mi} = \sum_{i=1}^{N} 2\pi R_i \cdot r_i^2, i = 1, 2, 3, ..., N \quad (2)$$

where R_i is the distance from the center line of the i-th bone matrix ring (counting from the inside to the outside)

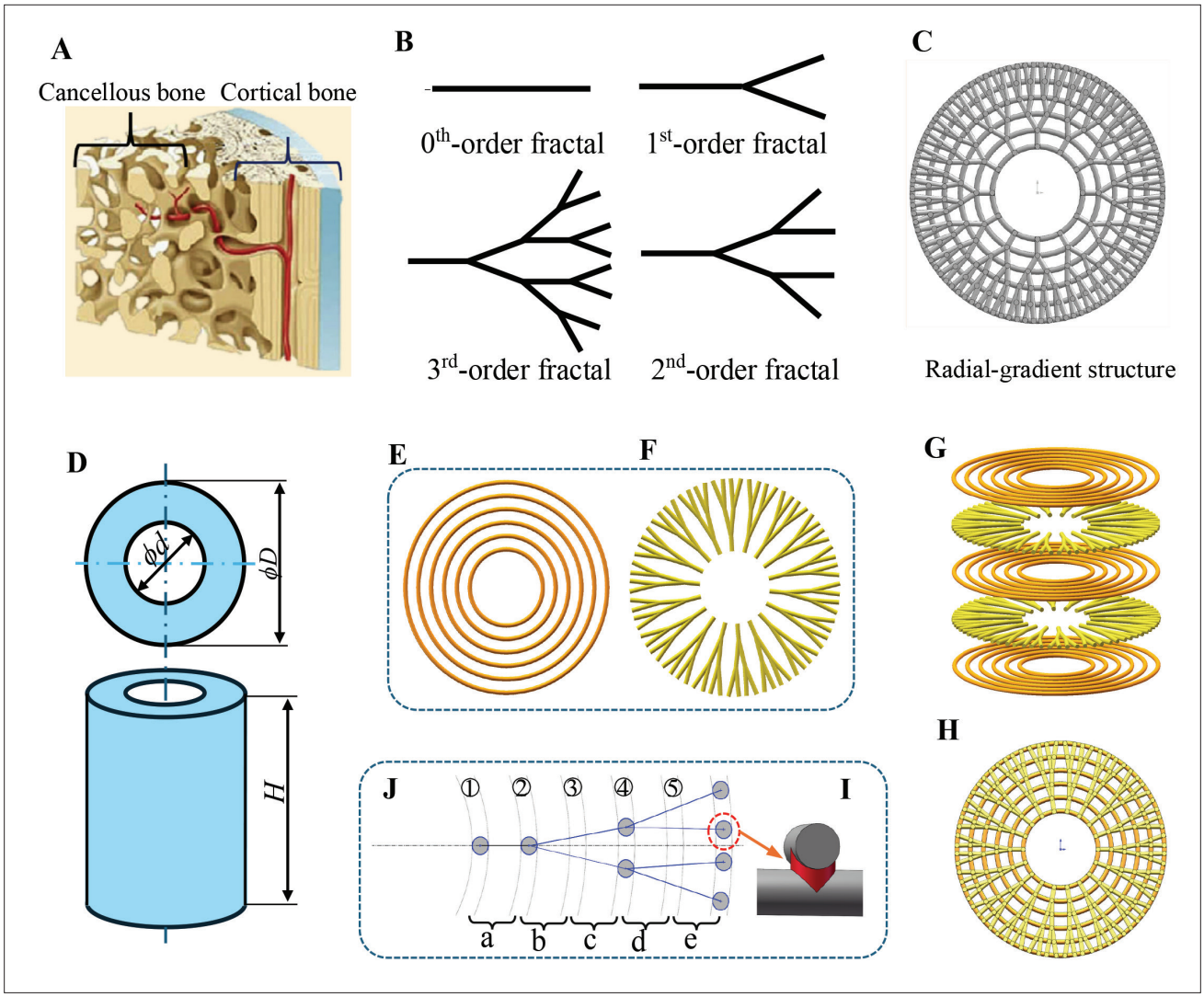

Figure 2. Schematic illustrations for designing tree-like fractal scaffolds. (A) Microstructure of human bone, (B) tree-like fractal curves with 0th-order, 1st-order, 2nd-order, and 3rd-order fractal, (C) radial-gradient structure from cancellous bone to cortical bone, (D) the geometric dimensions of the bone scaffold, (E) concentric ring-shaped bone matrix layer, (F) radial bone trabecular layer, (G) the bottom-up stacking of bone matrix layer and bone trabecular layer, (H) axial view of biomimetic scaffold, (I) 2nd-order tree like fractal structure and radial region division, and (J) the crisscross connection structure between bone matrix and trabeculae.

to the center of the bionic bone, and r_i is the radius of the i-th bone matrix ring.

The calculation for the volume V_{bc} of a bone trabecular network with a circular cross-section is as follows in **Equation (3)**:

$$V_{bc} = \sum_{j=0}^{n} V_{jbc} = \sum_{j=0}^{n} m_j \pi \left(\frac{d_j}{2}\right)^2 l_j = \frac{\pi}{4} d_0^2 l_0 \frac{1-(m\gamma\mu)^{n+1}}{1-m\gamma\mu} \quad (3)$$

where, m_j, d_j, and l_j are the number of bifurcations, diameter, and length of the j-th order trabecular, respectively.

The overall porosity k of the biomimetic scaffold can be determined using **Equations (2)** and **(3)**. The calculation is as follows in **Equation (4)**:

$$k = 1 - NV_{bc} - V_m \quad (4)$$

where k is the porosity of the scaffold.

2.2. Optimization problem

The stress-shielding effect is a key challenge for bone implants. Traditional dense metal implants have an elastic modulus significantly higher than that of natural bone tissue, leading to excessive physiological load on the prosthesis and complications such as bone resorption and prosthesis loosening. Natural bone tissue exhibits high strength and low modulus.[2,39] Therefore, maintaining sufficient strength to withstand loads during daily activities while reducing the modulus of bone implants is a key issue in the design of porous bone scaffolds. Based on this, this study aims to reduce stress shielding in porous scaffolds and achieve a synergy between their modulus and strength. The optimization goal is to minimize the effective Young's modulus and maximize the yield strength of porous scaffolds, and to conduct multi-objective optimization of the structural dimensions of a tree-like fractal bionic scaffold. Firstly, using the biomimetic scaffold design process (Figure 2), feasible design spaces were extracted based on the defect-site structure and biological constraints, and porous scaffolds with different fractal parameters were then designed. The scaffolds were fabricated using the selective laser melting (SLM) process, and their mechanical and biological properties were analyzed. Secondly, the fractal structure with favorable mechanical and biological properties was selected as the research object, and the porous scaffolds with different geometric parameters were created. Then, based on FE mechanics calculations, the effective Young's modulus (E_e) and yield strength (Y_s) of the porous scaffold were obtained, and a dataset was obtained. The optimal design set was selected from the target space according to the multi-objective optimization results. Finally, based on the tree-like fractal scaffold obtained through the multi-objective optimization, the correlation of the multi-objective optimization design was verified through experimental testing. In this article, E_e is referred to as the "effective Young's modulus" or "Young's modulus" of the scaffold, which can be used interchangeably with "stiffness."

The definition of the problem of minimizing the effective Young's modulus and maximizing the yield strength of porous bone scaffolds with predefined fractal parameters is shown in **Equation (5)**.

$$\begin{aligned} &\text{Maximize:} \quad E_e \\ &\text{Minimize:} \quad Y_e \\ &\text{Subject to:} \\ &\qquad \theta: \ [20^\circ, 30^\circ] \\ &\qquad d_h: \ [0.3, 0.7] \\ &\qquad N: \ [3, \ 6] \\ &\qquad d_j: \ [0.3, 0.7] \end{aligned} \quad (5)$$

where θ is the fractal angle of the tree-like fractal structure; d_h is the diameter of the annular bone matrix in mm; N is the number of concentric rings of the annular bone matrix; and d_j is the diameter of radial bone trabeculae in mm.

2.3. Optimization methods

2.3.1. Orthogonal design and sensitivity calculation

The orthogonal test method is a statistical method that scientifically arranges multi-factor experiments through orthogonal arrays. It enables efficient analysis of multiple factors and multiple levels with a small number of representative experiments, and its core advantage lies in significantly reducing the number of experiments through a test design characterized by "uniform dispersion and neat comparability."[40] To avoid difficulties in fitting caused by differences in the dimensions of dependent variables, all data must undergo normalization processing, and the formula is show in **Equation (6)**:

$$X_i = -1 + 2 \times \frac{x_i - x_{min}}{x_{max} - x_{min}} \quad (6)$$

where X_i is the normalized index value of the i-th test, x_i is the index value of test i, and x_{max} and x_{min} are the maximum and minimum index values among all tests in the orthogonal array, respectively.

Based on the design process of the tree-like fractal scaffold and the experimental analysis of its mechanical properties, the specific structural parameters of the porous bone scaffold to be optimized were determined.

Orthogonal design experiments were conducted using four parameters: fractal angle θ, diameter of the annular bone matrix ring d_h, number of concentric bone matrix rings m, and radial trabecular diameter d_j. Three levels were determined for each factor, as shown in Table 1.

To reduce the number of experiments and computational complexity, an L9(4^3) orthogonal table was established based on the four-factor, three-level design requirements using the orthogonal experimental design method. A total of nine experiments were conducted.[41] Then, based on the nine different structural parameters listed in the orthogonal table, corresponding porous scaffold models with tree-like fractal structures were established.

To compare and analyze the influence of structural parameters of tree-like fractal porous scaffolds on optimization objectives, the response values of each experiment were obtained based on the porous scaffold model. Using the variance-based sensitivity analysis method, the sensitivity index for each design variable to the response was measured. The calculation method for the sensitivity of the i-th optimization variable to the j-th optimization objective, denoted as $S_j(X_i)$, is shown in **Equation (7)**[42]:

$$S_j(X_i) = \frac{V[E(Y_j/X_i)]}{V(Y_j)} \tag{7}$$

where Y_j is the j-th optimization objective, X_i is the i-th optimization parameter, $E(Y_j/X_i)$ is the average value of Y_j when X_i is fixed, $V[E(Y_j/X_i)]$ is the variance of $E(Y_j/X_i)$, and $V(Y_j)$ is the variance of the Y_j.

2.3.2. Multi-objective optimization algorithm

Based on the structural parameters of the porous tree-like fractal scaffold obtained by the orthogonal experimental design method, the corresponding porous scaffold models were established, and a dataset for multi-objective optimization calculation was obtained through FE simulation calculation. Then, the PSO-BP-NSGAIII integrated algorithm was used to optimize the optimal eigenvalue parameters of the tree-like fractal scaffold. Specifically, the GA and PSO algorithms were adopted to optimize the weights and thresholds of the BP neural network, and the NSGA III was employed to perform multi-objective optimization on the optimal structural eigenvalues of the tree-like fractal porous scaffold.

The BP neural network is a multi-layer feedforward network trained by the error BP algorithm.[43] The main approach of the GA optimization is to perform crossover and mutation on thresholds and weights, followed by fitness calculation and selection of optimal ones. Since the initial weights and thresholds of the BP neural network are random arrays, they affect the prediction correlation of the entire network. Thus, its weight and threshold must be optimized. The GA was utilized to optimize the BP neural network, and the Levenberg–Marquardt algorithm was employed for local optimization to obtain the global optimal solution.[44] PSO is a method for searching for optimal solutions. The initial weights and thresholds of the BP neural network were defined as particles in the particle swarm, and all particles form a group. The basic idea of the PSO algorithm is to find the optimal solution through cooperation and information sharing among individuals in the group.[45]

The calculations of particle velocity and position are shown in **Equations (8)** and **(9)**:

$$V_{i(n+1)} = \omega V_{i(n)} + C_1 * rand * (gbest - X_{i(n)}) + C_2 * rand * (zbest - X_{i(n)}) \tag{8}$$

where $V_{i(n+1)}$ is the velocity of the i-th particle in the $(n+1)$-th iteration; C_1 is the global learning factor; C_2 is the individual learning factor; ω is the iteration weight; *rand* is a random number of [0,1]; *gbest* is the globally optimal X value, and *zbest* is the individually optimal X value.

$$X_{i(n+1)} = X_{i(n)} + V_{i(n+1)} \tag{9}$$

where $X_{i(n+1)}$ represents the specific position of the i-th particle in the $(n+1)$-th iteration.

Table 1. Levels of factors used in the orthogonal design experiments

Factors \ Levels	Level 1	Level 2	Level 3
Fractal angle θ (°)	20	25	30
Diameter of the annular bone matrix d_h (mm)	0.4	0.5	0.6
Number of concentric rings of bone matrix N	4	5	6
Radial trabecular diameter d_j (mm)	0.4	0.5	0.6

The NSGA-III can perform multi-objective fitness comparisons, which distinguishes it from the GA. NSGA III replaces congestion calculation with the reference point method for optimization based on the NSGA II algorithm, avoiding getting stuck in local optima.[46] Therefore, the NSGA III algorithm was applied to the multi-objective optimization in this study.

2.4. Finite element analysis for scaffold Young's modulus

The effective Young's modulus of the porous scaffold was calculated using the Abaqus software (version 2021, Dassault Corp., USA), and its boundary conditions are shown in Figure 3. Both the upper and lower steel plates were treated as rigid bodies; the lower plate was fixed. The compressive strain was sufficiently small to ensure that the stress and strain of the entire scaffold remain within the elastic region. The upper steel plate was uniformly loaded along the Z-axis at a speed of 0.5 mm/min, with a loading displacement of 5% of the specimen height, which is consistent with the compression test. Friction hard contact was used between the porous scaffold and the rigid plate, and the penalty coefficient was set to 0.2.[24] Due to the central-axis symmetry of the porous bone scaffold, 1/4 of the model was used for the compression analysis. The mesh type adopted was quadratic tetrahedral elements of type C3D10. Through mesh independence calculation and size optimization, the final mesh size was determined to be 0.07 mm. In this FE analysis, the bone scaffold material was Ti6Al4V. Its material parameters were as follows: elastic modulus of 113.8 GPa, Poisson's ratio of 0.32, density of 4430 kg/m^3, and yield strength of 970 MPa.[47] The material parameters of the upper and lower steel plates were: Poisson's ratio of 0.29, elastic modulus of 193 GPa, and a density of 7930 kg/m^3.

According to the FE method, the reaction force was calculated and converted into stress. The effective Young's modulus calculation formula for the scaffold is as follows in **Equation (10)** [24]:

$$Ee = \frac{RF/A_{\text{ave}}}{\varepsilon} = \frac{RF/[(1-k)A_{\text{c}}]}{\Delta L/L_0} \quad (10)$$

where A_{ave} is the average cross-sectional area of the scaffold perpendicular to the compression direction, A_c is the total cross-sectional area perpendicular to the compression direction (excluding pores), ε_0 is the compressive strain, k is the porosity of the scaffold, and ΔL and L_0 are the length change and initial length of the scaffold in the compression direction, respectively.

2.5. Computed fluid dynamics analysis for scaffold permeability

In addition to bearing loads, the porous structure of bone scaffolds plays an essential role in nutrient transport in damaged areas. To evaluate the mass-diffusion capacity of the scaffold, permeability is defined as an intrinsic property of the scaffold that determines the liquid flow rate through it. In this study, the permeability of porous scaffolds was calculated using CFD software (version 2022 R1, ANSYS, USA). Due to the symmetrical structure of the porous scaffold, a 1/4 model of the scaffold was selected for simulation calculation. The CFD simulation model and boundary conditions for the tree-like fractal scaffold are shown in Figure 4. To ensure consistency with the actual service conditions, the parameters of human body fluids were used to simulate the real surrounding flow environment of the porous scaffold in the human body.[36] The specific fluid parameters were as follows: viscosity in

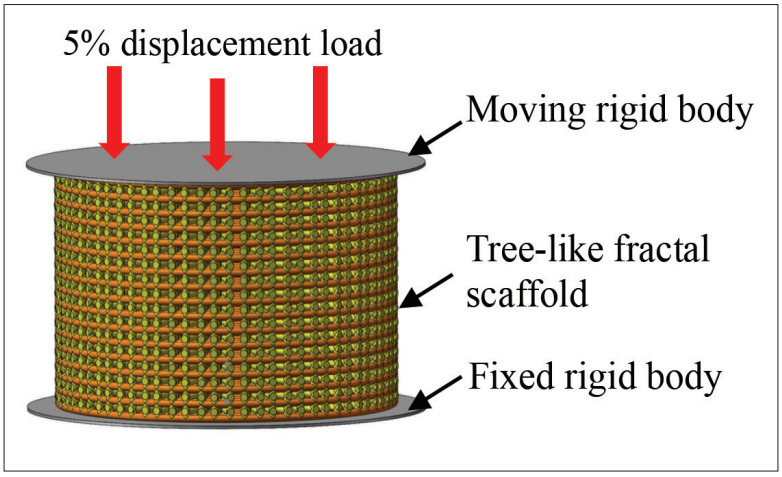

Figure 3. Schematic diagram of finite element compression calculation.

the fluid region μ = 0.0035 Pa·s, inlet flow velocity v_i = 0.01 m/s, outlet pressure P_{outer} = 0 Pa, and no sliding on the support wall. By simulating the steady-state fluid flow inside the scaffold, the pressure drop ΔP between the inlet and outlet of the scaffold was calculated using **Equation (11)**, and the permeability was calculated using Darcy's law (**Equation [12]**)[47]:

$$\Delta P = P_{inner} - P_{outer} \quad (11)$$

$$k = \frac{\mu \cdot v_i \cdot L}{\Delta P} \quad (12)$$

where k is the permeability of the scaffold (m^2), μ is the viscosity of human body fluids (Pa·s), v_i is the inlet velocity of the fluid (m/s), L is the characteristic length of the fluid model in the direction of fluid flow (m), ΔP is pressure difference, and P_{inner} and P_{outer} are the pressures at the inlet and outlet of the scaffold (Pa), respectively (Figure 4).

2.6. Fabrication of biomimetic scaffolds

Ti6Al4V exhibits excellent biocompatibility and is widely used in bone implants.[47,48] Therefore, Ti6Al4V was selected for the preparation of tree-like fractal porous scaffolds. The Ti6Al4V metal powder is spherical in morphology, with a particle size of 15–45 μm and a Hall flowability of 45S. The scaffolds were fabricated using the 3D printing equipment BLT-S210 (Xi'an Bright Laser Technologies, China). Computer-aided design models of the porous scaffolds were modeled in SolidWorks 2023 and then converted to STL file format. The main process parameters for SLM 3D printing were a laser power of 120 W, a hatch spacing of 70 μm, a layer thickness of 30 μm, a scan speed

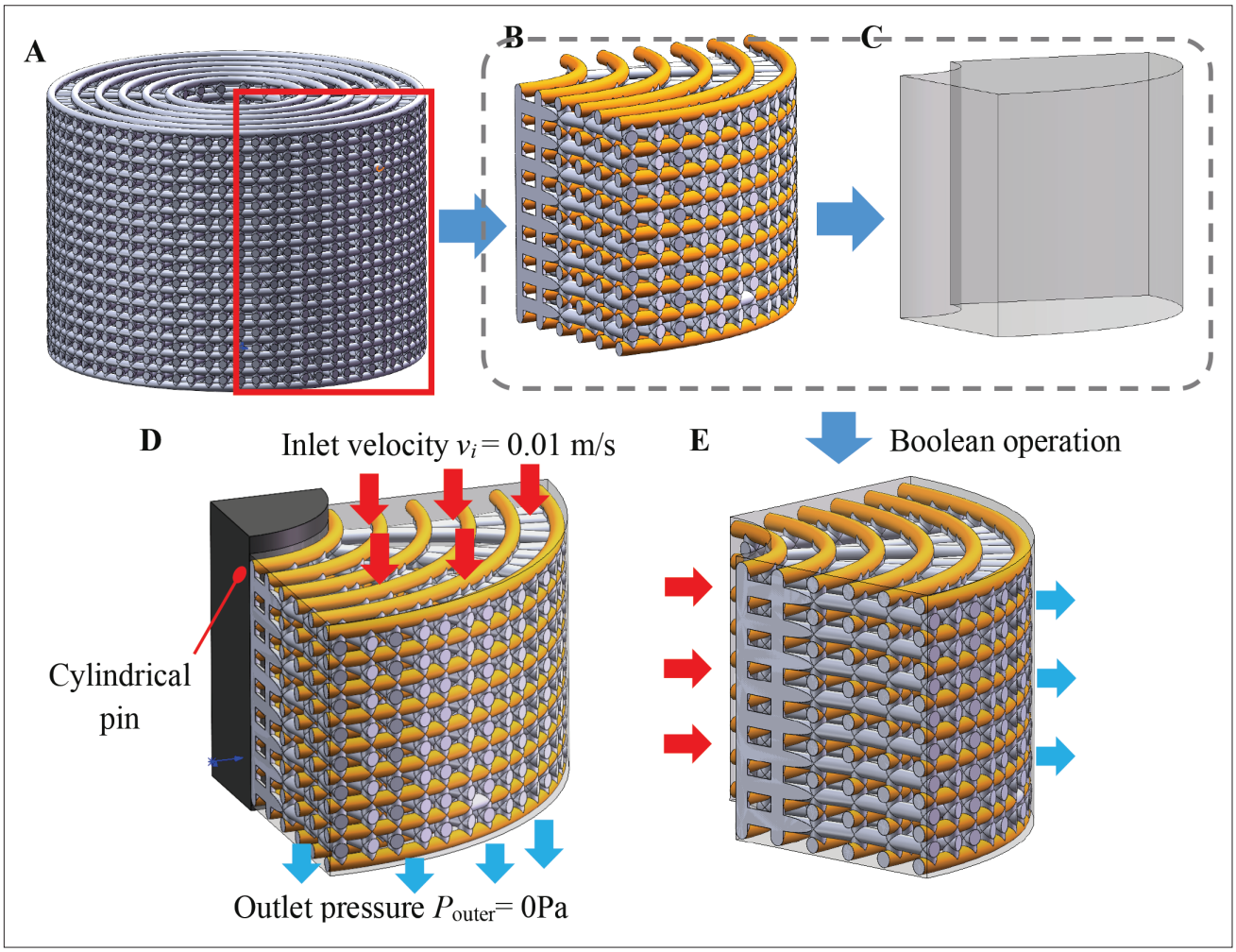

Figure 4. Schematic diagram of the computed fluid dynamics (CFD) fluid simulation. (A) The tree-like fractal scaffold model, (B) the 1/4 model, (B) the fluid domain model, (D) the CFD calculation model for axial permeability, and (E) the CFD calculation model for radial permeability (v_i is inlet velocity, P_{outer} is outlet pressure).

of 800 mm/s, and a laser spot size of 60 μm. The rotation angle between adjacent layers during printing was 67°, and the entire preparation process was performed under full argon conditions. After SLM 3D printing was completed, a wire cutting machine was used to cut the sample from the substrate. To ensure the mechanical properties of the sample, thermal stress treatment was performed to eliminate residual stress. The process was as follows: an annealing treatment was carried out at 650°C for 120 min, and heating was conducted at a rate of 10°C/min from 25 to 650°C. Furthermore, to remove the unmelted Ti6Al4V powder from the sample surfaces, anhydrous ethanol was used for ultrasonic cleaning. To minimize the impact of the preparation process on the accuracy of sample preparation, all scaffolds were fabricated using the same material and process. The tree-like fractal porous biomimetic scaffold prepared by SLM is shown in Figure 5, with geometric dimensions D = 24 mm, d = 8 mm, and h = 16.5 mm.

2.7. Mechanical properties testing

Mechanical property testing was conducted to compare and analyze the influence of fractal parameters on the mechanical properties of tree-like fractal biomimetic scaffolds. Additionally, to evaluate the correctness of FE calculations, the FE calculation results were compared with the test results. The test equipment used was a DF13.105T universal testing machine (Sinotest Equipment, China), and the testing standard referred to ISO 13314–2011.[49] The sample was placed at the center of the workbench and the upper plate downward to compress the sample, with no restrictions on the lateral expansion, as shown in Figure 6A. Loading rate of 0.5 mm/min, and the compression test was stopped when the sample fractured. During the compression process, the variation history of force with displacement was recorded, and the stress–strain curve was obtained. Then, the Young's modulus (E_e), yield strength (Y_s), and compressive strength (σ_c) of tree-like fractal scaffolds were obtained. E_e was determined by the slope of the straight line within the elastic region of the stress–strain curve, Y_s was determined by the intersection of the stress–strain curve at a 0.2% offset line parallel to the elastic line, and the σ_c was obtained through the first peak stress in the curve (Figure 6B).[50]

Due to the different structures of the four fractal scaffolds, their masses also varied. For a more scientific comparative analysis, we performed normalization on the masses of the four fractal scaffolds. The normalization calculation process is as follows in **Equations (13)–(15)**:

$$V_{total} = \pi \cdot \left(\frac{D}{2}\right)^2 \cdot h - \pi \cdot \left(\frac{d}{2}\right)^2 \cdot h \tag{13}$$

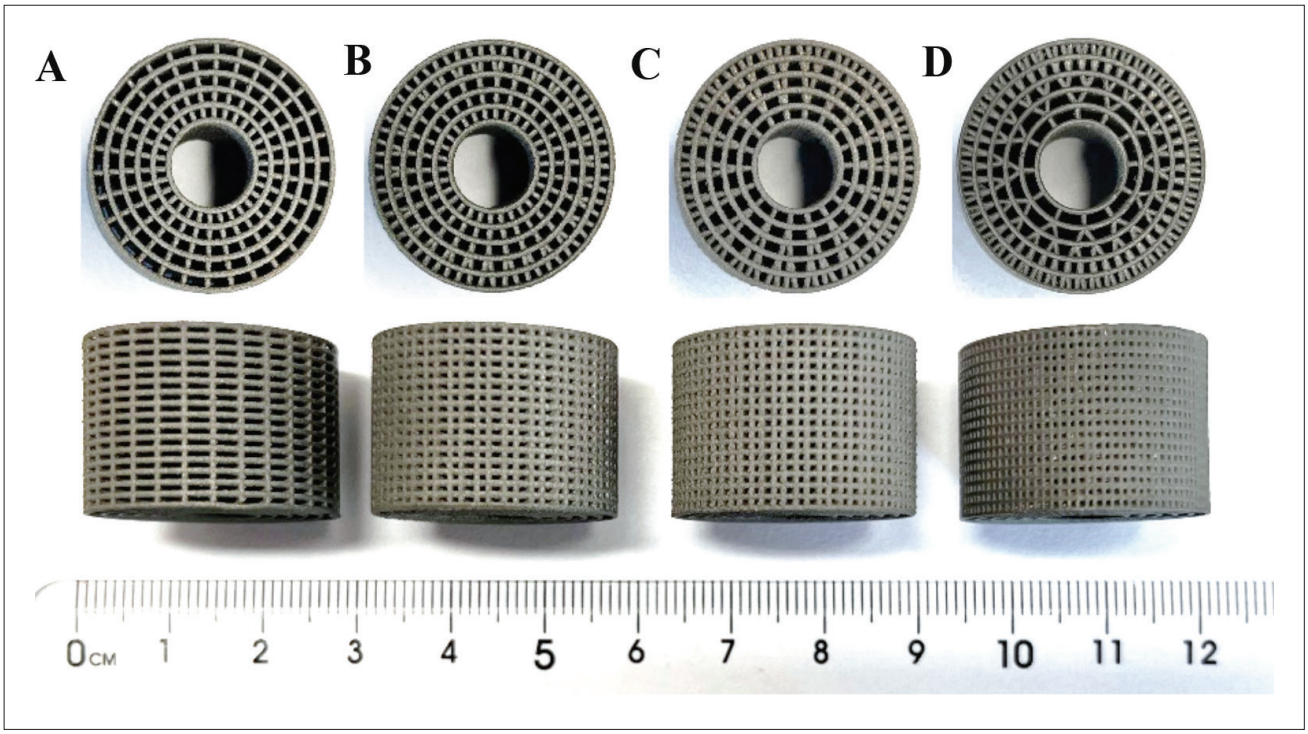

Figure 5. Tree-like fractal scaffolds fabricated using selective laser melting three-dimensional printing. (A) 0th-order scaffold, (B) 1st-order scaffold, (C) 2nd-order scaffold, and (D) 3rd-order scaffold.

where D is the outer diameter of the cylinder (mm), d is the inner diameter of the cylinder (mm), and h is the initial height of the sample (mm)

$$\rho_t = \frac{m}{V_{\text{total}}} \tag{14}$$

where m is the mass of the fractal scaffold (g).

$$\rho_r = \frac{\rho_t}{\rho_m} \tag{15}$$

where ρ_m is the density of Ti6Al4V material and ρ_m = 0.00443 g/mm^3.

Lastly, each stress data point on the original stress–strain curve was divided by the relative density (ρ_r) of the corresponding specimen.

3. Results and discussion

3.1. Effects of fractal parameters on porosity

The distribution of porosity along the radial direction is shown in Figure 7. In Figure 7, a, b, c, d, and e correspond to the local regions of the porous scaffold (Figure 2J) and the porosity within those regions, respectively. In the 0th-order fractal model, the radial porosity distribution showed that the internal region had lower porosity, while the external region had a larger one (Figure 7A), which is opposite to the radial porosity distribution of natural bone. The porosity of the 1st-order fractal scaffold along the radial direction showed a distribution in which the middle region had the largest porosity, while the inner and outer regions had the smallest porosities (Figure 7B). The porosity of 2nd-order and 3rd-order fractal scaffolds exhibited approximately linear distributions along the radial direction (Figure 7C,D), with a gradually decreasing gradient from the inner to the outer region, which is similar to that of natural bone.[51] In the 2nd-order fractal model, the porosities of the inner and outer regions were 74% and 67%, respectively. In the 3rd-order fractal model, the porosities of the inner and outer regions were 77% and 63%, respectively. The larger porosity in the inner region is similar to that of cancellous bone. In comparison, the smaller porosity in the outer region is similar to that of cortical bone (Figure 2A).

The above findings indicate that, through a tree-like fractal design, bionic bone scaffolds with a radial porosity gradient can be obtained by adjusting fractal parameters. In clinical applications, porous scaffolds can be designed with porosity matching the gradient distribution of the patient's bone defect site by optimizing fractal parameters, thereby better satisfying the personalized requirements of patients for implants.

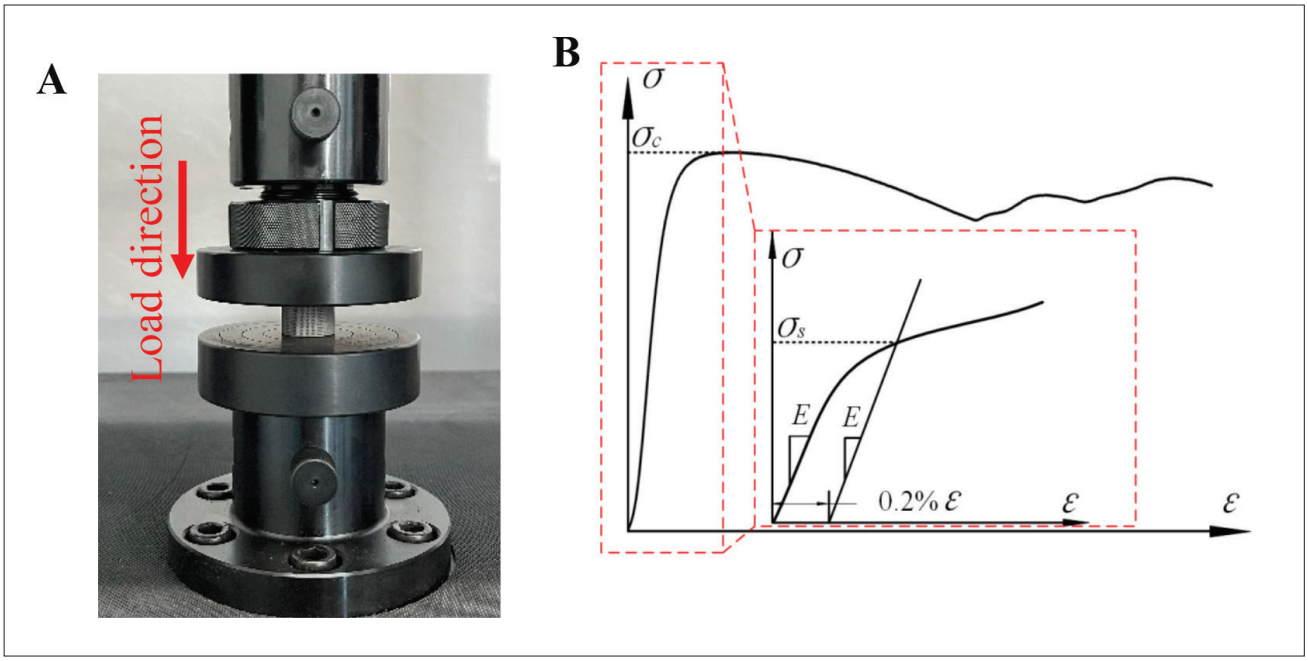

Figure 6. Mechanical properties testing and parameters calculation. (A) Compression testing, and (B) schematic of elastic modulus and strength.

3.2. Effects of fractal parameters on mechanical properties

To comparatively analyze the influence of fractal parameters on the mechanical properties of the scaffolds, quasi-static compression experiments were conducted on samples with different fractal parameters. A total of 20 samples were tested (five per type). Considering the differences in mechanical response and for the convenience of comparative analysis, only the mean stress–strain curves were plotted, as shown in Figure 8A. In the inception phase, the curve showed an elastic response until the yield point was reached. A small nonlinear phase appeared before the linear elastic phase, which is due to the establishment of complete contact between the plate and the sample. According to the measurement method for elastic modulus and yield strength in **Section 2.7** (Figure 6B) and the normalized stress–strain response curves (Figure 8A), the normalized yield strength and Young's modulus of the four groups of specimens were obtained as shown in Figure 7B and C. It is shown that under the condition of the same structural size parameters, the normalized yield strength of the 2nd-order fractal structure was the largest. Among the models with fractal structures, the 3rd-order fractal structure had the smallest normalized Young's modulus (13.602 GPa), followed by the 2nd-order fractal structure with a normalized Young's modulus of 15.424 GPa. However, the normalized yield strength of the 2nd-order fractal structure was significantly higher than that of the 3rd-order fractal structure. The comprehensive analysis of the test results shows that the 2nd-order tree-like fractal scaffold exhibited high yield strength and low Young's modulus, similar to the mechanical properties of natural bone, and can effectively reduce the risk of stress shielding. Furthermore, the comparison between the FE simulation results and the test results (Figure 8C) shows that the normalized Young's modulus calculated by the FE simulation was larger than the test results, with only a small difference. For example, the Young's modulus calculated by the FE of the 2nd-order fractal scaffold was 6.9% larger than the average of the test results. The Young's modulus calculation results for the four scaffolds showed small fluctuations and no significant differences, indicating the reliability of the FE simulation.

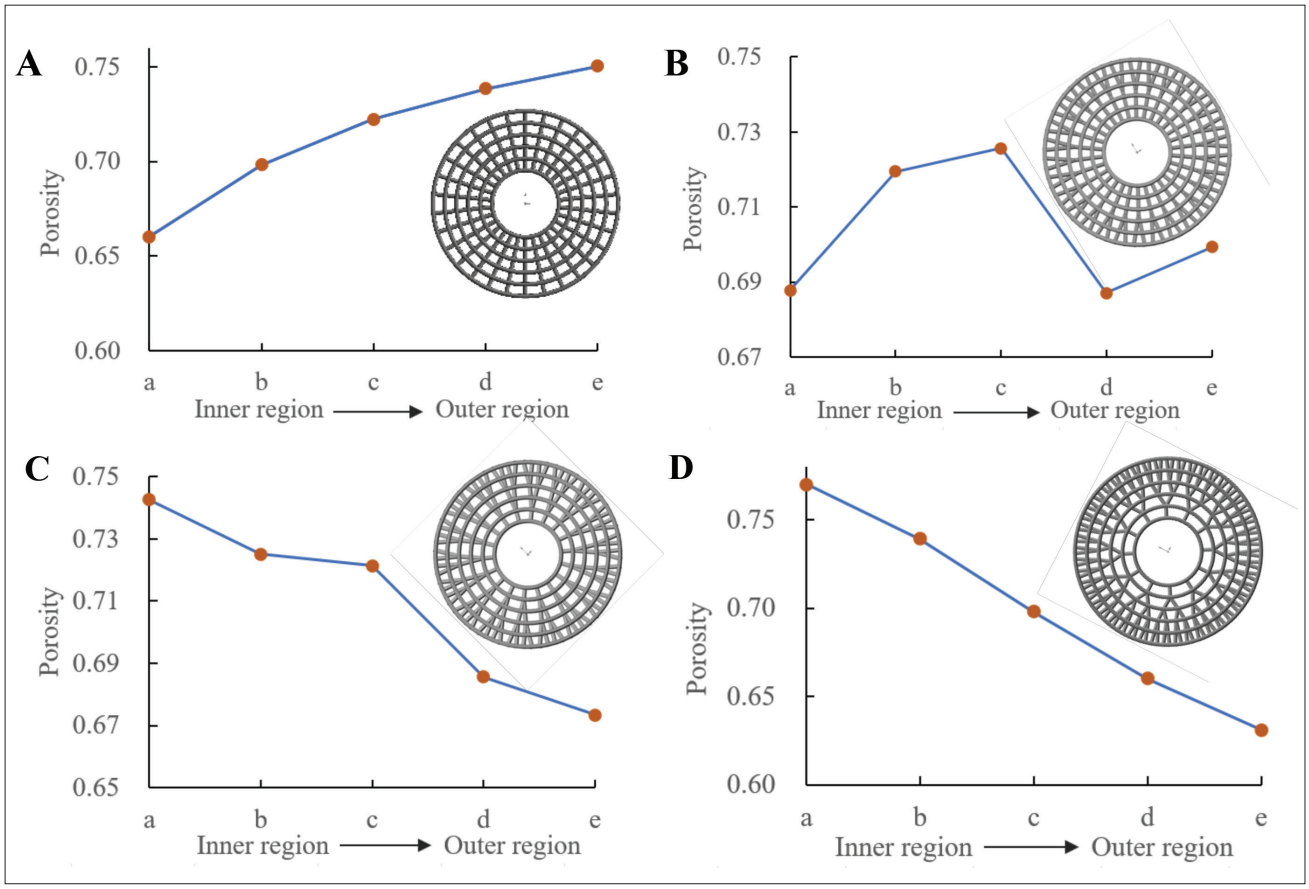

Figure 7. Radial distribution of porosity in porous scaffolds. (A) 0th-order fractal, (B) 1st-order fractal, (C) 2nd-order fractal, and (D) 3rd-order fractal.

The above findings indicate that tree-like fractal scaffolds exhibited high strength and low Young's modulus, characteristics consistent with those of natural bone, and can effectively reduce the risk of stress shielding. In addition, fractal parameters directly affect the mechanical properties of tree-like fractal scaffolds. Under the condition of equal strain, there were significant differences in the compressive stress of samples with different fractal structures. By optimizing fractal parameters, bone implants with different mechanical properties can be designed, making the Young's modulus and yield strength of bone implants closer to that of native bone.

3.3. Effects of fractal parameters on permeability

The CFD simulation results of the four porous scaffolds with different fractal parameters are shown in Figures 9 and 10. According to Darcy's law, the axial and radial permeabilities of the four models are shown in Figure 11. From the contour maps of the flow velocity distribution (Figures 9 and 10), it is evident that the distribution shows significant differences. The axial permeabilities of the 2nd-order and 3rd-order fractal scaffolds exhibited a strong fluid flow gradient from the inside to the outside, indicating that fractal parameters significantly affect the flow velocity distribution. Among the four different fractal structures, the 2nd-order tree-like structure had the maximum axial and radial permeability, while the 1st-order fractal structure had the minimum axial and radial permeability (Figure 11). Furthermore, the total permeabilities of the four fractal models from the 0th-order to the 3rd-order were as follows: 1.81×10^{-8} m^2, 1.31×10^{-8} m^2, 3.13×10^{-8} m^2, and 2.56×10^{-8} m^2. The 2nd-order fractal scaffold had the optimal comprehensive permeability, followed by the 3rd-order fractal model. The comprehensive permeability of the 2nd-order was 22.2% higher than that of the 3rd-order, thereby effectively improving cell diffusion.[24] According to the porosity distribution in **Section 3.1**, the porosities of the 2nd-order and 3rd-order fractal structures showed

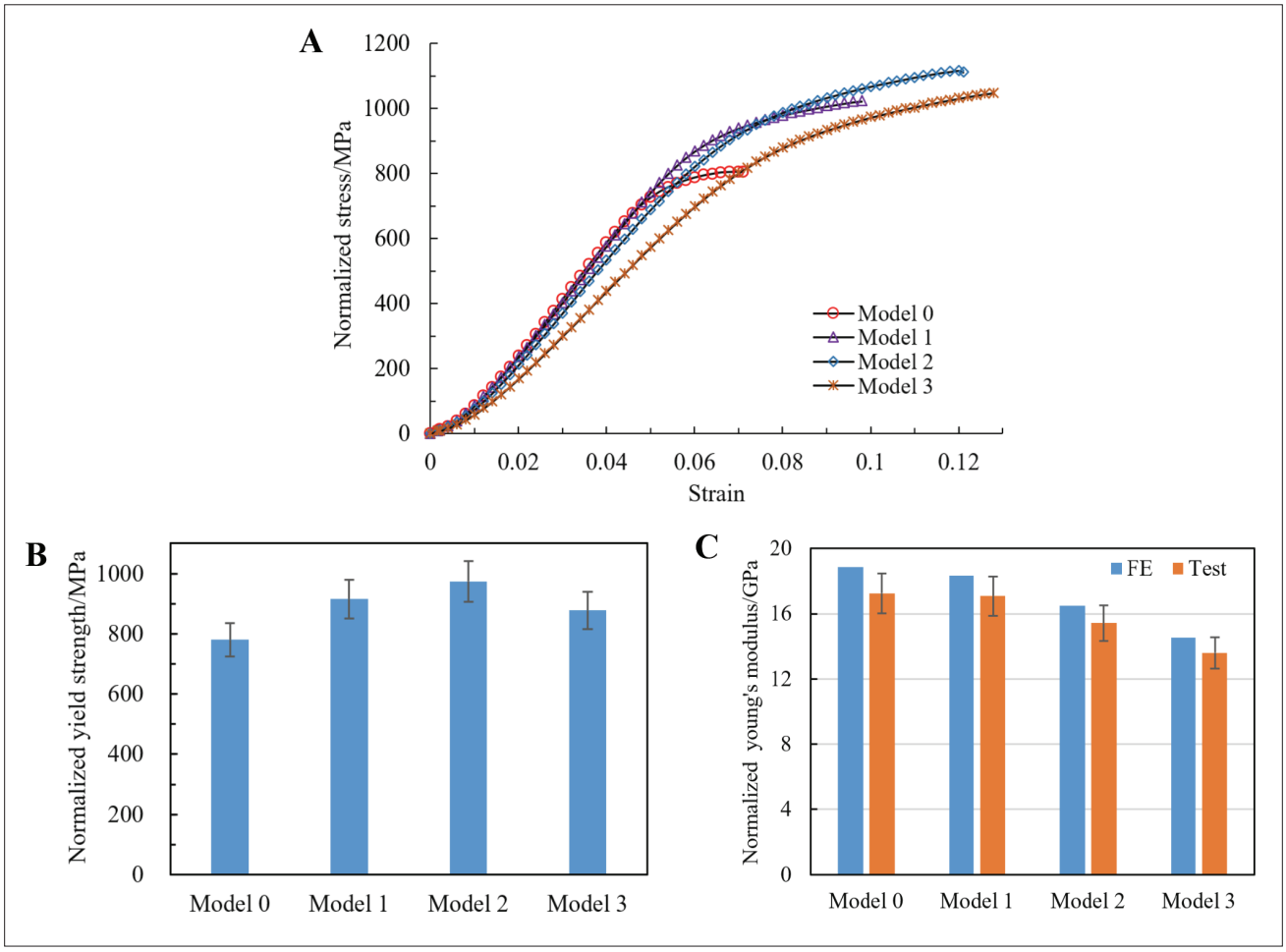

Figure 8. Mechanical properties test results. (A) Mean stress–strain curves of fractal scaffolds, (B) the yield strength of the scaffold, and (C) the Young's modulus of the scaffold. Note: Model 0, Model 1, Model 2, and Model 3 in the figure correspond to the 0th-order to 3rd-order fractal models, respectively. Abbreviation: FE, finite element.

a uniform gradient change from the inside to the outside. Therefore, the greater internal porosity can significantly improve the scaffold's permeability and offset the impact of reduced edge porosity, thereby enabling the radial-gradient porous scaffold to exhibit better permeability.

These findings indicate that 2nd-order fractal scaffolds exhibit good fluid-flow gradients and optimal overall permeability. The fractal parameters directly affect the distribution of flow velocity and permeability. In practical applications, by adjusting the fractal parameters, porous scaffolds with different permeability can be designed to better promote the bone regeneration process.

3.4. Orthogonal design calculation and sensitivity analysis

According to the experimental and FE calculation results in **Section 3.2**, the design of porous scaffolds with high yield strength and low elastic modulus can be achieved by optimizing the fractal parameters. The 2nd-order fractal scaffold exhibited good permeability (**Section 3.3**), and the Young's modulus of the 2nd-order fractal structure was approximately equal to that of the 3rd-order fractal structure. Since the 2nd-order fractal structure is simpler than the 3rd-order fractal structure, the 2nd-order fractal structure was selected as the research object for multi-objective optimization. Based on the L9(4^3) orthogonal design, nine tree-like fractal porous scaffold models with different structural parameters were created. The Young's modulus and yield strength corresponding to each porous scaffold were obtained through FE calculations. Each set of calculated data was entered into the corresponding positions to complete the design calculation of the orthogonal table, as shown in Table 2. The orthogonal design results in Table 2 were used as the dataset for subsequent neural network training.

The sensitivity indices of the four design variables to the response values were calculated using the variance-

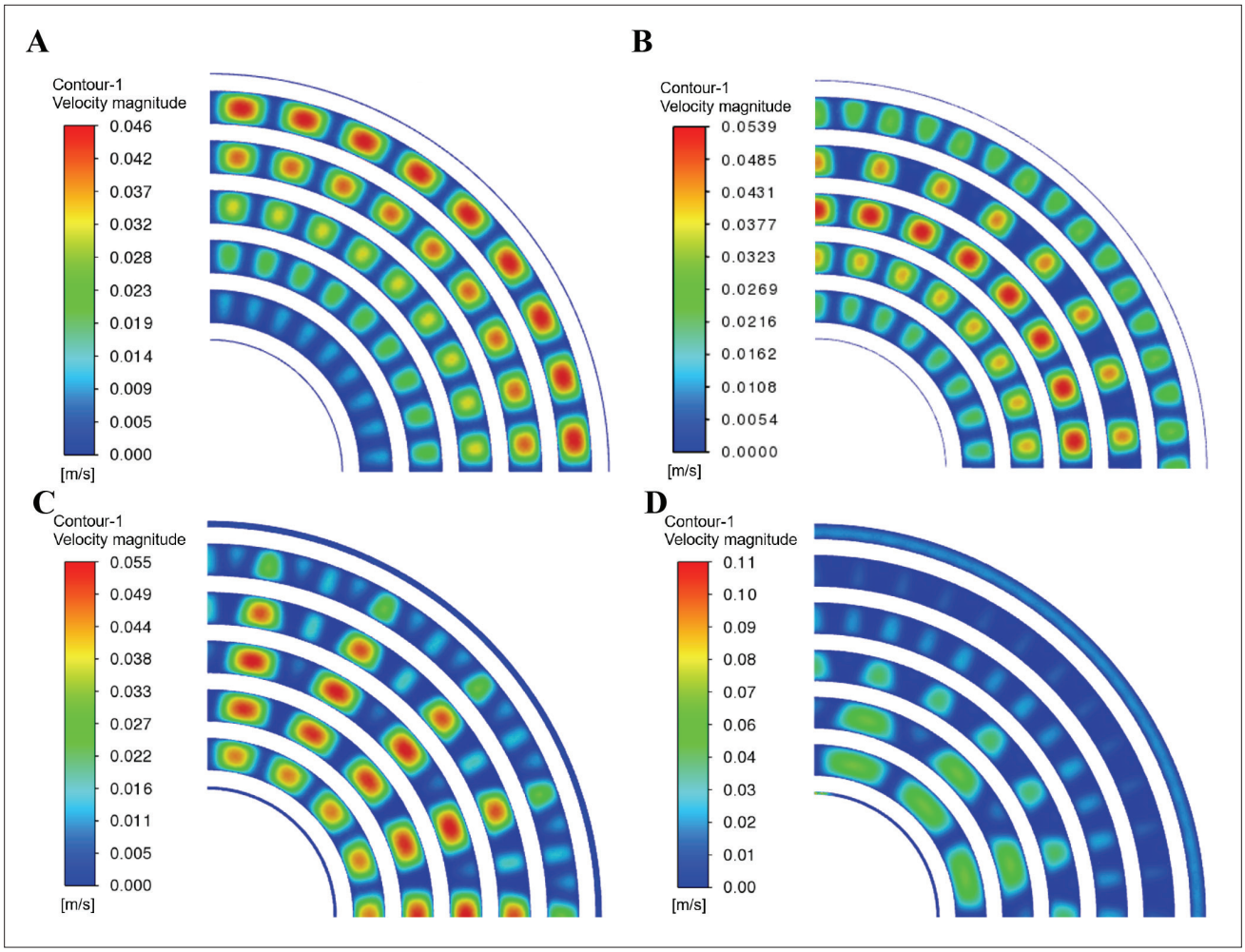

Figure 9. Cloud chart of axial flow velocity distribution. (A) 0th-order model, (B) 1st-order model, (C) 2nd-order model, and (D) 3rd-order model.

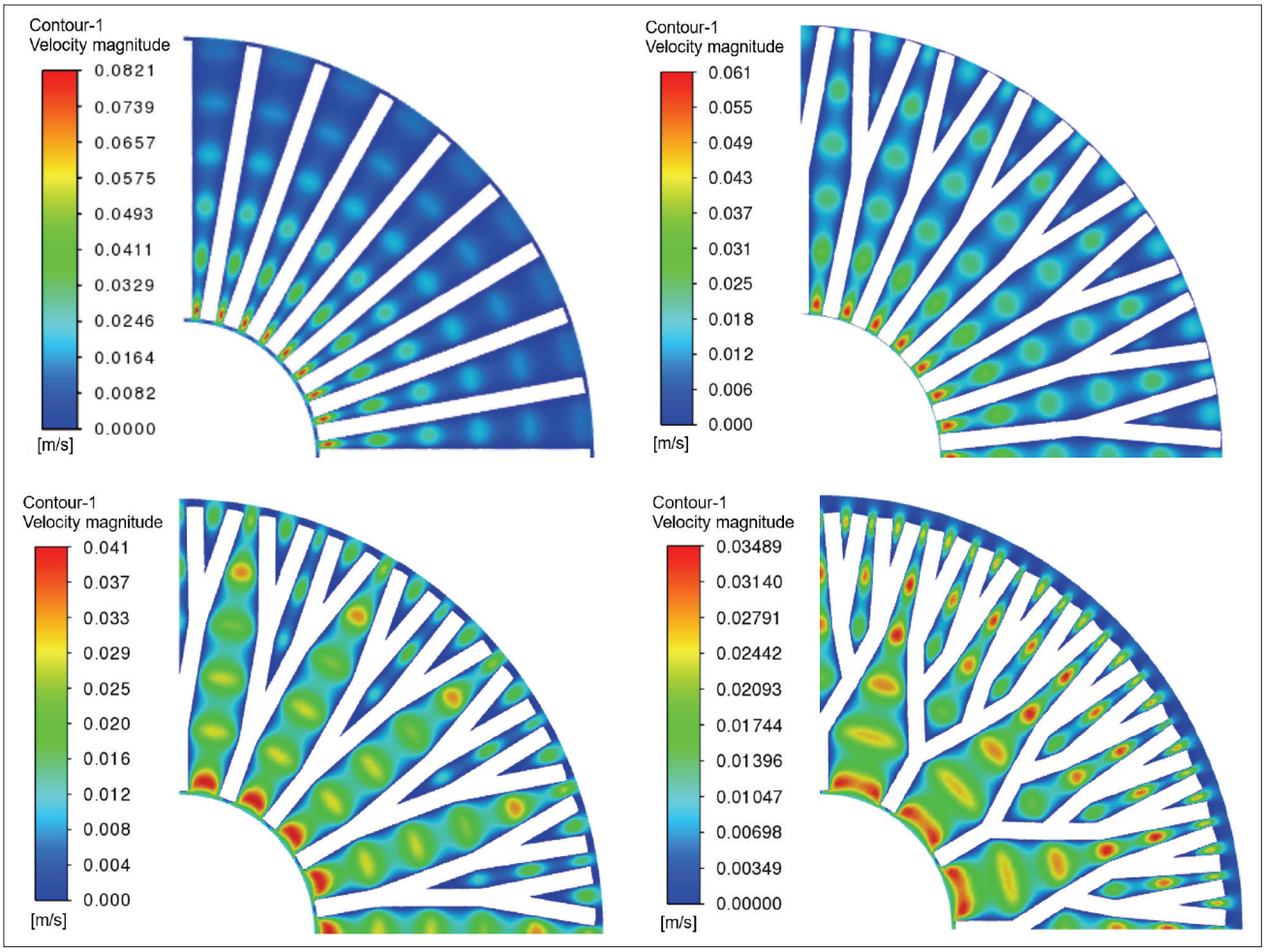

Figure 10. Cloud chart of radial flow velocity distribution. (A) 0th-order model, (B) 1st-order model, (C) 2nd-order model, and (D) 3rd-order model.

based sensitivity analysis method, as shown in Table 3. The sensitivity index of the fractal angle θ to the Young's modulus of the scaffold was 0.108, and its sensitivity index to the yield strength was 0.098. The sensitivity index of the annular bone matrix diameter d_h to Young's modulus was 0.465, and its sensitivity index to yield strength was 0.536, which is the most significant sensitivity index among the four design variables. Furthermore, both the number of concentric rings of the bone matrix N and the radial trabecular diameter d_j significantly impacted the sensitivity index of the scaffold. The four design variables selected in this study had varying degrees of influence on the scaffold's Young's modulus and yield strength. Therefore, it was reasonable to use Table 2 as the dataset for subsequent neural network training.

3.5. Algorithm optimization of the backpropagation neural network

Random initial thresholds and weights in the BP neural network negatively affected fitting correlation. Therefore, the GA was used to optimize the initial thresholds, while PSO was used to optimize the initial weights. The GA-BP neural network was subsequently used for training, and the PSO-BP neural network was used to perform multi-objective fitting on the dataset (Table 2). Root-mean-square errors (RMSEs) for multi-objective prediction were obtained, as shown in Figure 12. For GA-BP, when predicting Young's modulus, the RMSE of the training and test sets were 0.857 and 4.671, respectively (Figure 12A). When predicting yield strength, the RMSEs for the training and test sets were 9.889 and 48.729, respectively (Figure 12B). For PSO-BP, when predicting Young's modulus, the RMSEs of the training and test sets were 0.112 and 3.068, respectively (Figure 12C). When predicting yield strength, the RMSEs for the training and test sets were 1.119 and 32.314, respectively (Figure 12D). When PSO-BP and GA-BP were used to predict Young's modulus, the differences in RMSE between the training and test sets were relatively small. However, in the prediction of yield strength, the RMSE of both the training set and

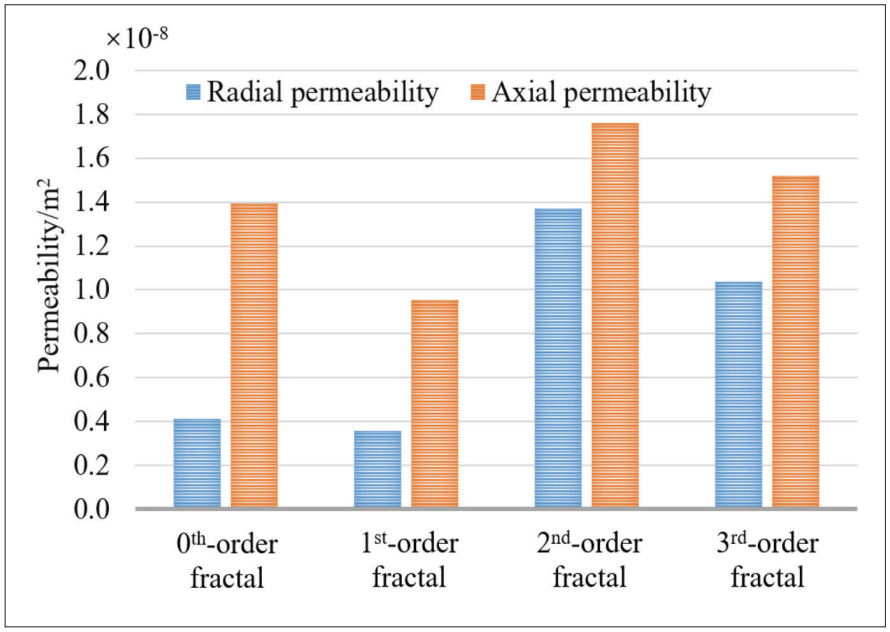

Figure 11. Axial and radial permeability of tree-like fractal porous scaffold.

Table 2. Orthogonal table corresponding to the nine tree-like fractal scaffolds

Number	Fractal angle θ (°)	Diameter of the annular bone matrix d_h (mm)	Number of concentric rings of bone matrix	Radial trabecular diameter d_j (mm)	Young's modulus E_e (GPa)	Yield strength Y_s (MPa)
1	20	0.4	4	0.4	7.439	82.894
2	20	0.5	6	0.5	18.216	190.386
3	20	0.6	5	0.6	17.119	185.603
4	25	0.4	6	0.6	14.095	126.843
5	25	0.5	5	0.4	12.555	132.859
6	25	0.6	4	0.5	12.035	124.034
7	30	0.4	5	0.5	10.661	111.981
8	30	0.5	4	0.6	18.395	152.903
9	30	0.6	6	0.4	18.716	177.534

Table 3. Sensitivity index of various variables

Name	Fractal angle θ (°)	Diameter of the annular bone matrix d_h (mm)	Number of concentric rings of bone matrix	Radial trabecular diameter d_j (mm)
Young's modulus, E_e (GPa)	0.108	0.465	0.255	0.173
Yield strength, Y_s (MPa)	0.098	0.536	0.285	0.081

test set fitted by PSO-BP were significantly smaller than those fitted by GA-BP. This indicates that the PSO-BP fit is considerably better than that of GA-BP.

The comparison of prediction correlation between GA-BP and PSO-BP is shown in Figure 13. The correlation coefficient for the training set relationship in GA-BP was 0.99797, while that for PSO-BP was 1, which is slightly higher than that for GA-BP. Both the PSO-BP and the GA-BP achieved a correlation coefficient of 1 in both the test and validation sets. The comprehensive fitting correlation coefficient of GA-BP was 0.783, while that of PSO-BP was close to 1, indicating that PSO-BP has a higher comprehensive fitting correlation coefficient.

The results comparison in Figures 12 and 13 shows that the RMSEs of both the training and test sets fitted by the PSO-BP were significantly smaller than those fitted by the GA-BP, indicating that the PSO-BP neural network has a better fitting effect. The training set fitting correlation

coefficient of the PSO-BP was slightly higher than that of the GA-BP, while the comprehensive fitting correlation coefficient of the PSO-BP (0.9998) was 27.72% higher than that of the GA-BP (0.78278). These results indicate that the prediction correlation coefficient of the BP neural network optimized by PSO is higher. Therefore, the PSO-BP neural network was selected to model the relationships among Young's modulus, yield strength, and the structural parameters of the tree-like fractal scaffold.

3.6. Multi-objective optimization and result verification

Based on the fitting results of the PSO-BP, the NSGA III was adopted to optimize the minimum value of the scaffold's Young's modulus and the maximum value of the yield strength. Based on the Pareto chart obtained from the multi-objective optimization, the optimal solution was determined by selecting the point with a smaller Young's modulus and a larger yield strength as the comprehensive optimal point, as shown in Figure 14. When the yield strength increased to 58.09 MPa, the decreasing amplitude of the minimum Young's modulus showed a significant weakening. Therefore, the point with a yield strength of 58.09 MPa and a Young's modulus of 5.965 GPa was selected as the optimal point (Figure 14). The structural dimension parameters of the tree-like fractal scaffold corresponding to this optimal point were obtained: fractal angle θ = 20.004° (rounded to 20°), diameter of the annular bone matrix d_h = 0.415 mm (rounded to 0.42 mm), number of rings of annular bone matrix N =4.17 (rounded

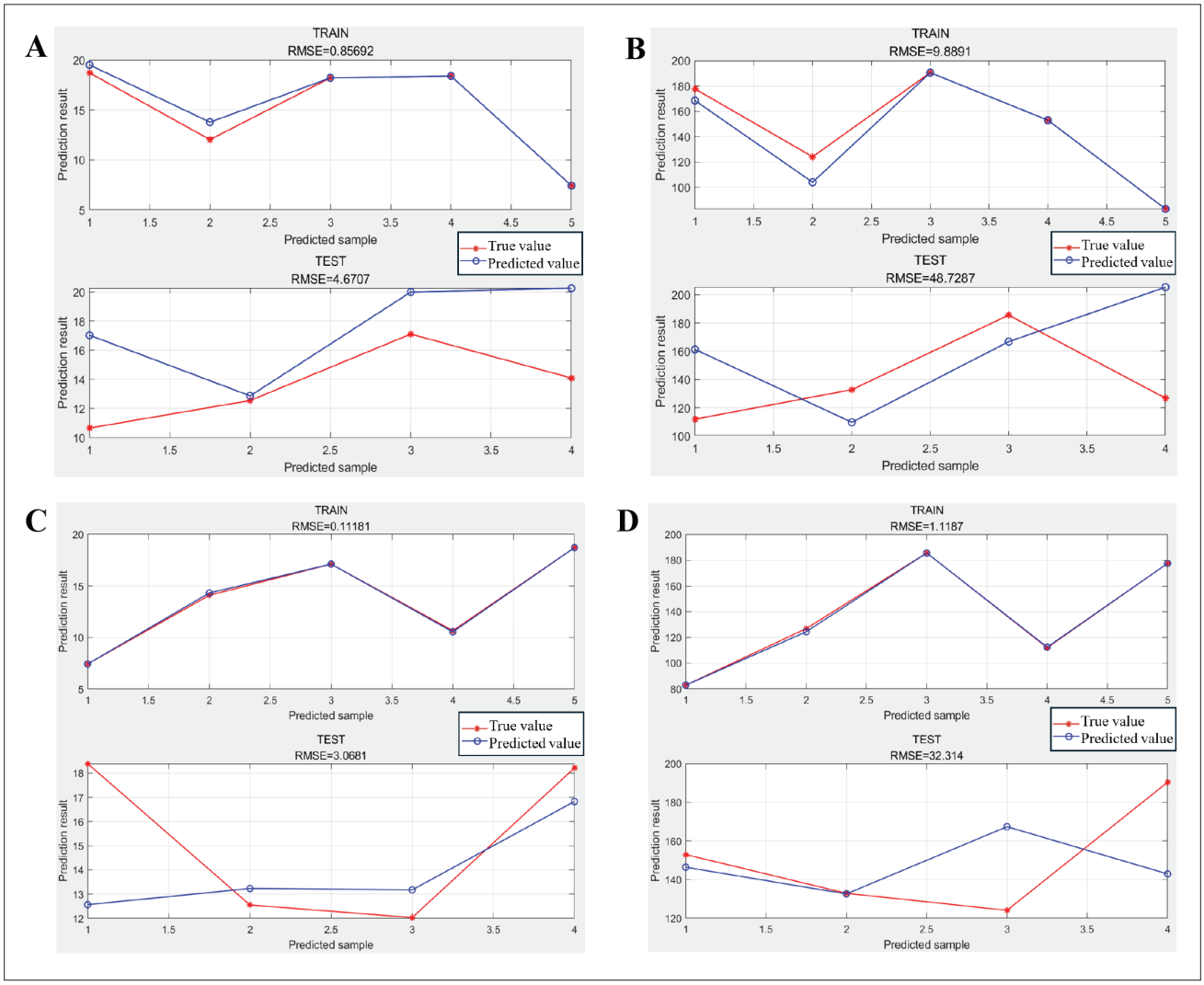

Figure 12. Root-mean-square error (RMSE) of neural network target prediction. (A) RMSE of genetic algorithm-back propagation (GA-BP) for Young's modulus prediction, (B) RMSE of GA-BP for yield strength prediction, (C) RMSE of particle swarm optimization (PSO)-BP for Young's modulus prediction, and (D) RMSE of PSO-BP for yield strength prediction.

to four), and radial trabecular diameter d_j = 0.3 mm. Based on the obtained key structural parameters of the 2nd-order tree-like fractal scaffold, an optimized 2nd-order tree-like scaffold model was established and fabricated using SLM 3D printing. Subsequently, mechanical experiments were conducted to verify the feasibility and correlation of the multi-objective optimization. The average stress–strain curve and performance parameters of the 2nd-order tree-like fractal scaffold after multi-objective optimization are shown in Figure 15.

The test value and predicted value of the Young's modulus of the optimized 2nd-order fractal scaffold were 5.965 and 6.438 GPa, respectively. The predicted and tested yield strengths were 58.09 and 58.576 MPa, respectively (Figure 15B). The difference between the tested value and the predicted value of Young's modulus was only 0.473 GPa; the tested value was 7.93% larger than the predicted value. The difference between the test value and the predicted value of yield strength was only 0.486 MPa, and the test value was 0.83% greater than the predicted value. It can be concluded that the PSO-BP-NSGA III integrated algorithm has strong reliability and predictive ability for tree-like fractal scaffolds.

4. Conclusion

This study aimed to achieve a synergistic effect among structure, modulus, and strength of porous scaffolds and to reduce stress shielding. A novel method for the design and optimization of porous bone scaffolds based on bionics and PSO-BP-NSGA III integrated algorithm was proposed.

The tree-like fractal biomimetic scaffold exhibited a radial porosity gradient similar to that of natural bone. The porosity of the 2nd-order and 3rd-order fractal scaffolds showed approximately linear distributions along the radial direction, with a radial gradient in porosity that gradually decreased from the inside to the outside.

The tree-like fractal scaffold can achieve effective synergy of high strength and low Young's modulus. The yield strength and Young's modulus of the porous scaffold can be effectively adjusted by optimizing the fractal order. Test and FE results showed that the 2nd-order fractal scaffold exhibited a significantly high yield strength and a low Young's modulus.

The 2nd-order fractal scaffold exhibited a favorable fluid flow gradient and good permeability. Among the four different fractal structures, the 2nd-order fractal structure showed the optimal axial and radial permeability, with a comprehensive permeability of 3.13×10^{-8} m^2, which was 22.2% higher than that of the 3rd-order fractal scaffold.

The PSO-BP showed a higher correlation with Young's modulus and yield strength for tree-like fractal scaffolds. In terms of target prediction RMSE, the RMSEs of both the training and test sets were significantly smaller for PSO-

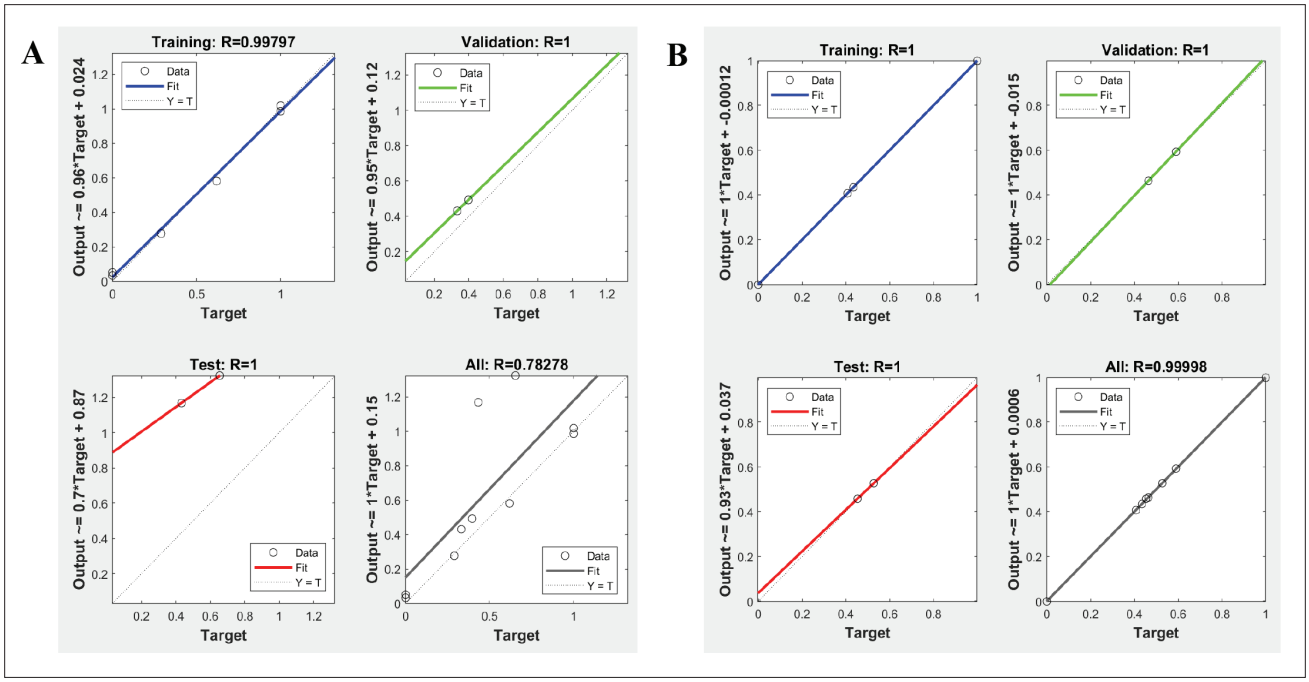

Figure 13. Prediction correlation of genetic algorithm-backpropagation (GA-BP) and particle swarm optimization (PSO)-BP. (A) Prediction correlation coefficient of GA-BP, and (B) prediction correlation coefficient of PSO-BP.

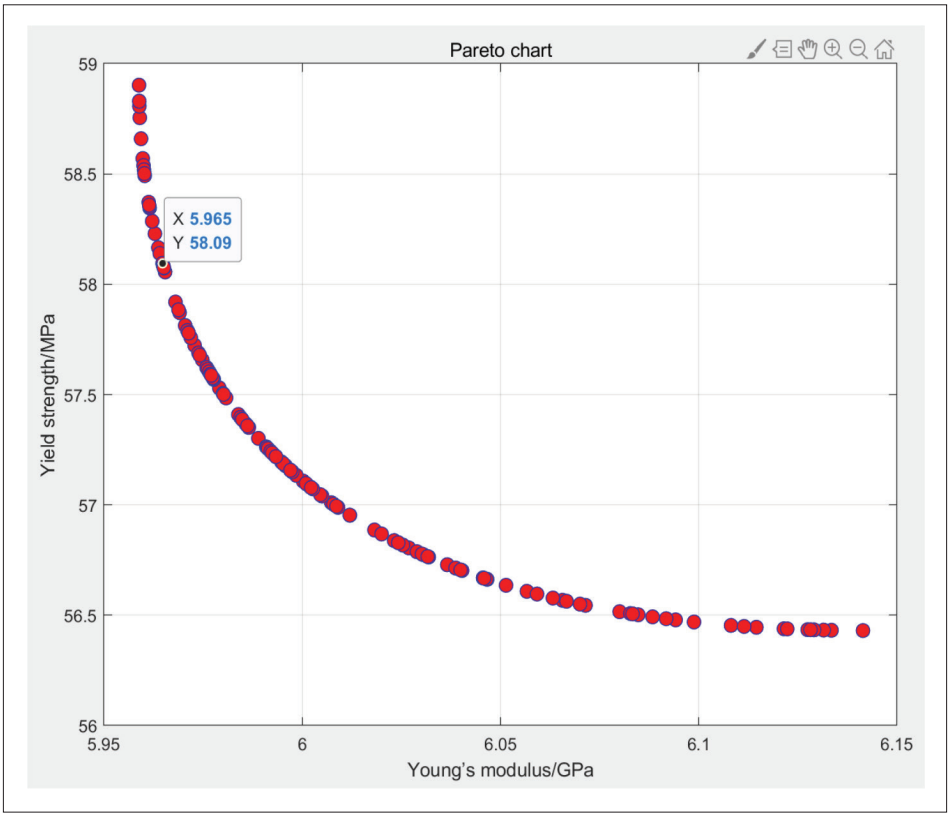

Figure 14. Pareto optimal solution set diagram.

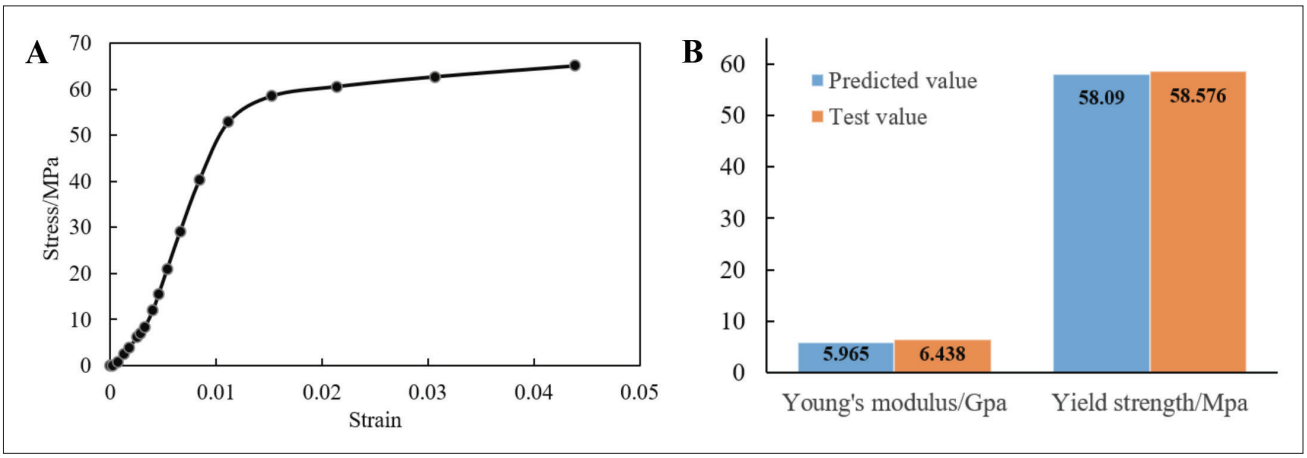

Figure 15. The mechanical properties of a 2nd-order tree-like fractal scaffold after multi-objective optimization. (A) Average stress–strain curve, and (B) yield strength and Young's modulus.

BP than for GA-BP. In terms of the prediction correlation coefficient, the comprehensive fitting correlation coefficient of the PSO-BP was close to 1, indicating a high overall fit.

The PSO-BP-NSGA Ⅲ integrated algorithm demonstrated high reliability and correlation in the multi-objective optimization of tree-like porous scaffolds. The tested value of Young's modulus was 7.93% larger than the predicted value. The measured yield strength was 0.83% higher than the predicted value, and the correlation between the prediction and the measured value was 99.17%.

Acknowledgments

None

Funding

This work was supported by the Natural Science Foundation of Chongqing Municipality (Grant no.: CSTB2023NSCQ-MSX0255), the Key Project of Science and Technology Research Program of Chongqing Education Commission (Grant no.: KJZD-K202203104), and the Science and Technology Research Program of Chongqing Education Commission (Grant no.: KJQN202403112).

Conflict of interest

The authors declare that there is no conflict of interest.

Author contributions

Conceptualization: Yuxi Liu, Aihua Li
Formal analysis: Hong Sun, Shuge Li
Investigation: Yuxi Liu, Aihua Li, Hong Sun
Methodology: Aihua Li, Yuxi Liu, Song Chen
Validation: Shuge Li, Aihua Li
Writing–original draft: Yuxi Liu, Aihua Li, Hong Sun
Writing–review & editing: Song Chen, Shuge Li, Hong Sun, Aihua Li

Ethics approval and consent to participate

Not applicable.

Consent for publication

Not applicable.

Availability of data

The data that support the findings of this study are available from the corresponding author upon reasonable request.

References

1. Luo L, Zheng W, Li J, *et al.* 3D-printed titanium trabecular scaffolds with sustained release of hypoxia-induced exosomes for dual-mimetic bone regeneration. *Adv Sci.* 2025;12(23):2500599.
doi: 10.1002/advs.202500599

2. Qin Y, Jing Z, Zou D, *et al.* A metamaterial scaffold beyond modulus limits: enhanced osteogenesis and angiogenesis of critical bone defects. *Nat Commun.* 2025;16:2180.
doi: 10.1038/s41467-025-57609-9

3. Jin Y, Li J, Fan H, Du J, He Y. Biomechanics and mechanobiology of additively manufactured porous load-bearing bone implants. *Small.* 2025;21(20):2409955.
doi: 10.1002/smll.202409955

4. Ahmed H, Shakshak M, Trompeter A. A review of the Masquelet technique in the treatment of lower limb critical-size bone defects. *Ann R Coll Surg Engl.* 2025;107(6): 383-389.
doi: 10.1308/rcsann.2023.0022

5. Naghavi SA, Tamaddon M, Garcia-Souto P, *et al.* A novel hybrid design and modelling of a customised graded Ti-6Al-4V porous hip implant to reduce stress-shielding: An experimental and numerical analysis. *Front Bioeng Biotechnol.* 2023;11:1092361.
doi: 10.3389/fbioe.2023.1092361

6. Li Z, Chen Z, Chen X, Zhao R. Design and evaluation of TPMS-inspired 3D-printed scaffolds for bone tissue engineering: enabling tailored mechanical and mass transport properties. *Compos Struct.* 2024;327:117638.
doi: 10.1016/j.compstruct.2023.117638

7. D'Andrea L, Gabrieli R, Milano L, *et al.* Elastic and failure characterization of hydroxyapatite TPMS scaffolds using a combined approach of ultrasound, compression tests and micro-CT based numerical models. *Acta Mater.* 2025;287:120776.
doi: 10.1016/j.actamat.2025.120776

8. Liu H, Chen H, Sun B, *et al.* Enhancing angiogenesis and osseointegration through a double gyroid Ti6Al4V scaffold with triply periodic minimal surface. *Bio-Des Manuf.* 2025;8(1):36-54.
doi: 10.1631/bdm.2400114

9. Men Y, Tang S, Chen W, Liu F, Zhang C. Design and performance study of bone trabecular scaffolds based on triply periodic minimal surface method. *J Biomed Eng.* 2024;41(3):584-594.
doi: 10.7507/1001-5515.202310005

10. Deng T, Li M, Gong S, *et al.* Voronoi as the optimal approach for strut-based bone scaffold design. *Int J Mech Sci.* 2025;295:110124.
doi: 10.1016/j.ijmecsci.2025.110124

11. Wu C, Wan B, Xu Y, *et al.* Dynamic optimisation for graded tissue scaffolds using machine learning techniques. *Comput Methods Appl Mech Eng.* 2024;425:116911.
doi: 10.1016/j.cma.2024.116911

12. Ibrahimi S, D'Andrea L, Gastaldi D, Rivolta MW, Vena P. Machine learning approaches for the design of biomechanically compatible bone tissue engineering scaffolds. *Comput Methods Appl Mech Eng.* 2024; 423:116842.
doi: 10.1016/j.cma.2024.116842

13. Liu W, Zhang Y, Lyu Y, Bosiakov S, Liu Y. Inverse design of anisotropic bone scaffold based on machine learning and regenerative genetic algorithm. *Front Bioeng Biotechnol.* 2023;11:1241151.
doi: 10.3389/fbioe.2023.1241151

14. Boccaccio A, Uva AE, Fiorentino M, Mori G, Monno G. Geometry design optimization of functionally graded scaffolds for bone tissue engineering: a mechanobiological approach. *PLoS One.* 2016;11(1):e0146935.

doi: 10.1371/journal.pone.0146935

15. Wu C, Wan B, Entezari A, Fang J, Xu Y, Li Q. Machine learning-based design for additive manufacturing in biomedical engineering. *Int J Mech Sci.* 2024;266:108828. doi: 10.1016/j.ijmecsci.2023.108828

16. Zhang J, Zhao J, Rong Q, Yu W, Li X, Misra RD. Machine learning guided prediction of mechanical properties of TPMS structures based on finite element simulation for biomedical titanium. *Mater Technol.* 2022;37(1):1-8. doi: 10.1080/10667857.2021.1999558

17. Liu G, Zhang X, Chen X, *et al*. Additive manufacturing of structural materials. *Mater Sci Eng R Rep.* 2021;145: 100596. doi: 10.1016/j.mser.2020.100596

18. Bie H, Chen H, Shan L, *et al*. 3D printing and performance study of porous artificial bone based on HA-ZrO2-PVA composites. *Materials (Basel).* 2023;16(3):1107. doi: 10.3390/ma16031107

19. Xu Q, Wang S, Bai Y, *et al*. Porous Ti3SiC2 ceramics with improved osteogenic functions via biomineralization as load-bearing bone implants. *J Mater Sci Technol.* 2024;195:248-259. doi: 10.1016/j.jmst.2024.01.025

20. Guo W, Li P, Wei Y, *et al*. Long ionic substitution through bredigite doping for microstructure and performance adjustment in DLP 3D-printed TPMS porous HA bone scaffolds. *Virtual Phys Prototyp.* 2024;19(1):e2423840. doi: 10.1080/17452759.2024.2423840

21. Li S, Yang H, Qu X, *et al*. Multiscale architecture design of 3D printed biodegradable Zn-based porous scaffolds for immunomodulatory osteogenesis. *Nat Commun.* 2024;15:3131. doi: 10.1038/s41467-024-47189-5

22. Min S, Wang C, Liu B, Lu D, Jin ZM. The biological properties of 3D-printed degradable magnesium alloy WE43 porous scaffolds via the oxidative heat strategy. *Int J Bioprint.* 2023;9(3):686. doi: 10.18063/ijb.686

23. Erica L, Giulia R, Stefania P, Silvia B, Alessandro F, Paolo C. Mechanical interaction between additive-manufactured metal lattice structures and bone in compression: implications for stress shielding of orthopaedic implants. *J Mech Behav Biomed Mater.* 2021;121:104608. doi: 10.1016/j.jmbbm.2021.104608

24. Foroughi AH, Razavi MJ. Multi-objective shape optimization of bone scaffolds: enhancement of mechanical properties and permeability. *Acta Biomater.* 2022;146:317-340. doi: 10.1016/j.actbio.2022.04.051

25. Li K, Liao R, Zheng Q, *et al*. Design exploration of staggered hybrid minimal surface magnesium alloy bone scaffolds. *Int J Mech Sci.* 2024;284:1109566. doi: 10.1016/j.ijmecsci.2024.109566

26. Wang Y, Qin X, Lv N, *et al*. Microstructure optimization for design of porous tantalum scaffolds based on mechanical properties and permeability. *Materials (Basel).* 2023;16:7568. doi: 10.3390/ma16247568

27. Paul R, Rana M, Gupta A, Banerjee T, Karmakar SK, Chowdhury AR. Design of biomimetic porous scaffolds for bone tissue engineering. *Transp Porous Media.* 2024;151:1453-1473. doi: 10.1007/s11242-024-02082-z

28. Liu Y, Cao Q, Yong S, *et al*. Optimal structural characteristics of osteoinductivity in bioceramics derived from a novel high-throughput screening plus machine learning approach. *Biomaterials.* 2025;321:123348. doi: 10.1016/j.biomaterials.2025.123348

29. Sorrentino A, Bianchi G, Radi E, Castagnetti D. Towards new strut-based auxetic meta-biomaterials for trabecular bone scaffolds. *Int J Eng Sci.* 2025;215:104316. doi: 10.1016/j.ijengsci.2025.104316

30. Xu Y, Zhang S, Ding W, *et al*. Additively-manufactured gradient porous bio-scaffolds: permeability, cytocompatibility and mechanical properties. *Compos Struct.* 2024;336:118021. doi: 10.1016/j.compstruct.2024.118021

31. Ma H, Men Y, Tang S, Hao P, Zhang C. Simulation analysis of strength and permeability of crystalline porous scaffolds. *Med Biomech.* 2024;39(2):222-228. doi: 10.16156/j.1004-7220.2024.02.005

32. Xu B, Lee K, Li W, *et al*. A comparative study on cylindrical and spherical models in fabrication of bone tissue engineering scaffolds: finite element simulation and experiments. *Mater Des.* 2021;211:110150. doi: 10.1016/j.matdes.2021.110150

33. Santos J, Pires T, Gouveia BP, *et al*. On the permeability of TPMS scaffolds. *J Mech Behav Biomed Mater.* 2023;142:105848. doi: 10.1016/j.jmbbm.2020.103932

34. Mamuti M, Chao L, Tian Z. Analysis of mechanical characteristics and permeability of TPMS and Voronoi porous structure for bone scaffold. *Comput Methods Biomech Biomed Engin.* 2025;28(14):2111-2124. doi: 10.1080/10255842.2024.2358378

35. Zhang X, Fang G, Leeflang S, Zadpoor AA, Zhou J. Topological design, permeability and mechanical behavior of additively manufactured functionally graded porous metallic biomaterials. *Acta Biomater.* 2019;84:437-452. doi: 10.1016/j.actbio.2018.12.013

36. Lv Y, Wang B, Liu G, *et al*. Design of bone-like continuous gradient porous scaffold based on triply periodic minimal surfaces. *J Mater Res Technol.* 2022;21:3650-3665. doi: 10.1016/j.jmrt.2022.10.160

37. Maconachie T, Leary M, Lozanovski B, *et al*. SLM lattice structures: properties, performance, applications and challenges. *Mater Des.* 2019;183:108137.

doi: 10.1016/j.matdes.2019.108137

38. Liu Y, Li A, Du B, He X. Design and properties research of radial gradient controllable biomimetic bone scaffold based on tree-liked fractal structure. *Chem Eng J.* 2024;499:156168. doi: 10.1016/j.cej.2024.156168

39. Chmielewska A, Dean D. The role of stiffness-matching in avoiding stress shielding-induced bone loss and stress concentration-induced skeletal reconstruction device failure. *Acta Biomater.* 2024;173:51-65. doi: 10.1016/j.actbio.2023.11.011

40. Li Z, Qian G, Shen Z, *et al*. Effects of operating parameters for low-grade heat driven thermo-electrochemical cells based on orthogonal experiments. *Appl Therm Eng.* 2024;243:122664. doi: 10.1016/j.applthermaleng.2024.122664

41. Tang L, Lai C, Tan L. Heat dissipation performance analysis and structure optimization of cooling channels for motors and controllers. *J Chongqing Univ Technol (Nat Sci).* 2023;37(2):104-112. doi: 10.3969/j.issn.1674-8425(z).2023.02.012

42. Chen S, Xu P, Liu Y. Design and multi-objective optimization of hairpin motor cooling system based on orthogonal design method and composite algorithm. *Appl Therm Eng.* 2025;259:124971. doi: 10.1016/j.applthermaleng.2024.124971

43. Zhang H, Hui JM. A back propagation neural network-based method for intelligent decision-making. *Complexity.* 2021;2021(1):610797. doi: 10.1155/2021/6610797

44. Biswas MAR, Robinson MD, Fumo N. Prediction of residential building energy consumption: a neural network approach. *Energy.* 2016;117:84-92. doi: 10.1016/j.energy.2016.10.066

45. Zhu C, Zhu J, Liu Y. Comparison of GA-BP and PSO-BP neural network models with initial BP model for rainfall-induced landslides risk assessment in regional scale: a case study in Sichuan, China. *Nat Hazards.* 2020;100(1):173-204. doi: 10.1007/s11069-019-03806-x

46. Papasani A, Devarakonda N. A novel feature selection algorithm using decomposition-based multi-objective guided honey badger algorithm (MO-GHBA) and NSGA-III. *Kuwait J Sci.* 2023;50(2):53-64. doi: 10.1016/j.kjs.2023.02.009

47. Qin Y, Wang Q, Shi C, Liu B, Ma S, Zhang M. Structural design and performance study of primitive triply periodic minimal surfaces Ti6Al4V biomimetic scaffold. *Sci Rep.* 2022;12(1):12759. doi: 10.1038/s41598-022-17066-6

48. Koju N, Niraula S, Fotovvati B. Additively manufactured porous Ti6Al4V for bone implants: a review. *Metals (Basel).* 2022;12(4):687. doi: 10.3390/met12040687

49. International Organization for Standardization. *ISO 13314: Compression Test for Porous and Cellular Metals*. Geneva: ISO; 2011.

50. Zhu J, Zou S, Mu Y, Wang J, Jin Y. Additively manufactured scaffolds with optimized thickness based on triply periodic minimal surface. *Materials (Basel).* 2022;15:7084. doi: 10.3390/ma15207084

51. Qu H, Han Z, Chen Z, *et al*. Fractal design boosts extrusion-based 3D printing of bone-mimicking radial-gradient scaffolds. *Research (Wash D C).* 2021;2021:9892689. doi: 10.34133/2021/9892689